

Properties of dense molecular gas along the major axis of M 82

FEI LI,^{1,2,3} ZHI-YU ZHANG,^{1,2} JUNZHI WANG,^{3,4} FENG GAO,⁵ SHANGHUO LI,⁶ JING ZHOU,^{1,2} YICHEN SUN,^{1,2} ZIYI GUO,^{1,2} AND SHU LIU⁷

¹*School of Astronomy and Space Science, Nanjing University, Nanjing 210093, People's Republic of China*

²*Key Laboratory of Modern Astronomy and Astrophysics (Nanjing University), Ministry of Education, Nanjing 210093, People's Republic of China*

³*Shanghai Astronomical Observatory, Chinese Academy of Sciences, 80 Nandan Road, Shanghai 200030, People's Republic of China*

⁴*School of Physical Science and Technology, Guangxi University, Nanning 530004, People's Republic of China*

⁵*Hamburger Sternwarte, Universitaet Hamburg, Gojenbergsweg 112, 21029, Hamburg, Germany*

⁶*Korea Astronomy and Space Science Institute, 776 Daedeokdae-ro, Yuseong-gu, Daejeon 34055, Republic of Korea*

⁷*CAS Key Laboratory of FAST, National Astronomical Observatories, Chinese Academy of Sciences, Beijing 100012, China*

(Accepted 31 May, 2022)

ABSTRACT

Dense gas is important for galaxy evolution and star formation. Optically-thin dense-gas tracers, such as isotopologues of HCN, HCO⁺, etc., are very helpful to diagnose excitation conditions of dense molecular gas. However, previous studies of optically-thin dense-gas tracers were mostly focusing on average properties of galaxies as a whole, due to limited sensitivity and angular resolution. M 82, a nearby prototype starburst galaxy, offers a unique case for spatially-resolved studies with single-dish telescopes. With the IRAM 30-m telescope, we observed the $J = 1 \rightarrow 0$ transition of H¹³CN, HC¹⁵N, H¹³CO⁺, HN¹³C, H¹⁵NC, and SiO $J = 2 \rightarrow 1$, HC₃N $J = 10 \rightarrow 9$, H₂CO $J = 2 \rightarrow 1$ toward five positions along the major axis of M 82. The intensity ratios of $I(\text{HCN})/I(\text{H}^{13}\text{CN})$ and $I(\text{HCO}^+)/I(\text{H}^{13}\text{CO}^+)$ show a significant spatial variation along the major axis, with lower values in the central region than those on the disk, indicating higher optical depths in the central region. The optical depths of HCO⁺ lines are found to be systematically higher than those of HCN lines at all positions. Furthermore, we find that the ¹⁴N/¹⁵N ratios have an increasing gradient from the center to the outer disk.

Keywords: Starburst galaxies; Interstellar medium; Star formation

1. INTRODUCTION

Observations show that star-formation activities are closely connected with dense molecular gas both in the Milky Way and in other galaxies. Heiderman2010,Lada2010,Lada2012. The dense molecular gas are directly involved into star formation activities, and it can be probed with molecular lines with critical densities (n_{crit}) greater than 10^4 cm^{-3} , such as multi- J transitions of HCN and HCO⁺ (Lada 1992; Kohno et al. 1999; Kennicutt & Evans 2012). With observations of HCN $J = 1 \rightarrow 0$ toward 65 galaxies, Gao & Solomon (2004) found a tight linear correlation between the luminosities of HCN $J = 1 \rightarrow 0$ and total infrared emission. However, most dense gas tracers are normally optically thick both in Galactic giant molecular clouds (GMCs) and in external galaxies (Wang et al. 2014; Meier et al. 2015; Jiménez-Donaire et al. 2017; Li et al. 2017, 2020). Therefore, there is a large uncertainty in estimating the dense gas mass from a single transition line of a high dipole moment molecule, which is similar to the issue of the CO-to-H₂ conversion factors (Narayanan et al. 2012; Bolatto et al. 2013).

Optically thin dense-gas tracers, such as the isotopologues of HCN and HCO⁺, could help better revealing dense gas properties in galaxies, such as volume density, temperature, and excitation conditions. One can determine optical depths of dense gas tracers, using their isotopologue line ratios (Henkel et al. 1998; Martín et al. 2010; Wang et al. 2014; Li et al. 2020). Because of their low abundances, isotopologue lines are mostly optically thin, and thus they can be used to accurately determine dense molecular gas properties and help study dense gas–star formation relations in different galaxies (Li et al. 2020).

In most galaxies, however, isotopologue lines of dense gas tracers are too faint to be detected. Only a few detections of such lines have been reported in nearby galaxies (Henkel et al. 1998; Wang et al. 2014, 2016; Tunnard et al. 2015; Li et al. 2020),

Table 1. Observed positions along the major axis of M82

Position	R.A. (J2000)	Dec. (J2000)	R_{GC} kpc
1	09:55:48	69:40:40	0.45
2	09:55:50	69:40:43	0.28
3(center)	09:55:53.1	69:40:41	0
4	09:55:55	69:40:50	0.23
5	09:55:57	69:40:55	0.42

Positions-1 and -2 locate in the SW lobe. Positions-4 and -5 locate in the NE lobe. R_{GC} is the distance from the Galactic Centre.

which either are limited within only the central regions of galaxies, or take global properties of galaxies as a whole (Wang et al. 2014; Li et al. 2020).

Toward one of the nearest starburst galaxy, M 82, Li et al. (2020) observed multi- J HCN lines in the central region. Intriguingly, they found that the line profiles of $H^{13}CN$ $J=1\rightarrow 0$ and $J=3\rightarrow 2$ are not consistent with each other. The $J=1\rightarrow 0$ and $J=3\rightarrow 2$ transitions of $H^{13}CN$ are dominated by the red-shifted and the blue-shifted velocity components, respectively. Because $H^{13}CN$ $J=3\rightarrow 2$ has a higher upper energy level and a higher critical density than those of $H^{13}CN$ $J=1\rightarrow 0$, such a difference may indicate velocity-dependent excitation conditions, isotope abundance variations, or exotic radiative transfer processes. It is natural to rise the following questions: How much would dense gas properties vary at different locations and velocity components of a galaxy? How would dense gas isotopologue abundances change along the galactic disk? What physical mechanisms would regulate dense gas properties on galactic scales?

To address these questions above, the best way is to obtain spatially resolved dense gas isotopologue measurements, with deep integration. In this paper, we present new IRAM 30-m observations of the ^{13}C and ^{15}N isotopologues of HCN, HCO^+ , and HNC, along the major axis of M 82. We describe observations and data reduction in Section 2. The new spectra, their intensities, optical depths, and abundance ratios are presented in Section 3. Section 4 discussed possible mechanisms that may dominant or bias these line ratios. Final conclusions are summarized in Section 5.

2. OBSERVATIONS AND DATA REDUCTION

Observations were performed with the IRAM 30-m telescope, at Pico Veleta, Spain during February 2019 (Project number: 186-18, PI: Feng Gao). A total number of four different pointings were used to sample the off-center region along the major axis of M82, with a typical pointing offset of $15''$. We list these pointing positions in Table 1 below. Figure 1 shows the observed four off-center positions overlaid on the velocity-integrated flux (moment 0) map of HCN (Salas et al. 2014), where positions-1 and -2 are located in the South-Western side of M 82 while positions-4 and -5 are located in the North-Eastern side (Aladro et al. 2011b).

The Eight Mixer Receiver (EMIR) with dual-polarization and the Fourier Transform Spectrometers (FTS) backend with a 8-GHz frequency coverage for each band and a 195-kHz spectral resolution were used. EMIR was configured to the mutual observing mode for both E-90 (at 3 mm) and E-150 (at 2 mm) receivers. To verify that the signal is from the sky frequency rather than radio-frequency interference (RFI) from the Earth or from the backend, two different local oscillator (LO) tuning setups were used during the observations (see Table 2).

All observations were performed with the wobbler switching mode, which has a beam throw distance of $\pm 60''$ and a switching frequency of 0.5 Hz. Telescope pointing was checked every two hours with nearby strong quasi-stellar objects, while focus was checked at the beginning of each observation.

The beam sizes of the IRAM 30-m telescope are approximately $29''$ and $16''$ at 87 GHz and 145 GHz, respectively. Typical system temperature are ≤ 100 K and ~ 120 K, at 3-mm and 2-mm band, respectively. The antenna temperature (T_A^*) is converted to the main beam temperature (T_{mb}), using $T_{mb}=T_A^* \times F_{eff}/B_{eff}$, where the forward efficiencies (F_{eff}) are 0.95 and 0.93, beam efficiencies (B_{eff}) are 0.81 and 0.74, at 3-mm and 2-mm band, respectively. Each spectrum was read out every 2 minutes. The on-source time ranges from 3.5 to 4 hours towards each position.

We adopt GILDAS/CLASS¹ (Pety 2005, GILDAS team 2013) to reduce all spectral data as the following order: First, we check all spectra by eye and removed questionable ones. Second, for each position we average all reliable spectra into one spectrum. We then fit a first-order polynomial baseline and subtract it from the averaged spectrum. Last, the baseline-subtracted spectra are smoothed to a velocity resolution of ~ 35 km s^{-1} .

¹ <http://www.iram.fr/IRAMFR/GILDAS>

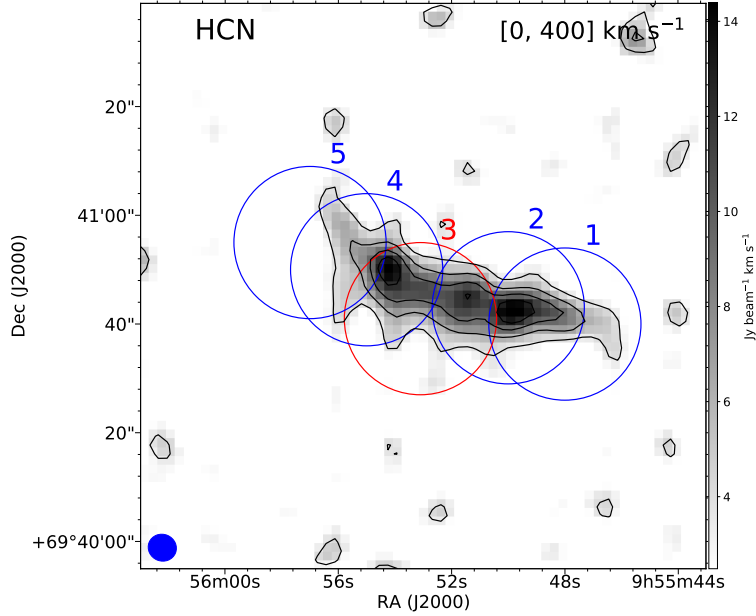


Figure 1. Velocity-integrated intensity (moment 0) maps of HCN $J=1\rightarrow 0$ emission from Salas et al. (2014) using CARMA. The synthesis beam of CARMA data has a FWHM of $\sim 6''$, which is shown in the lower left corner. IRAM 30-m beam ($29''$) coverage are shown in blue (off-centre) and red (central position; Li et al. (2020)) circles. The contours start from 3σ to 6σ , with an $1\text{-}\sigma$ level of 2.5 K km s^{-1} .

Table 2. The basic properties of these five positions

Position	Observing dates YYYY-MM-DD	$t_{\text{on source}}$ (min)	$T_{\text{sys}}^{3\text{mm}}$ (K)	$T_{\text{sys}}^{2\text{mm}}$ (K)	LO(3 mm) (GHz)	LO(2 mm) ^a (GHz)
Position-1	2019-Feb-06	47	83	120	86.34	146.97
	2019-Feb-07	20	93	130	86.29	146.92
	2019-Feb-10	48	110	–	86.15	–
Position-2	2019-Feb-06	26	93	120	86.34	146.97
	2019-Feb-07	25	94	127	86.29	146.92
	2019-Feb-08	39	105	–	86.24	–
	2019-Feb-09	26	106	–	86.19	–
Position-4	2019-Feb-06	22	96	134	86.34	146.97
	2019-Feb-07	25	90	121	86.29	146.92
	2019-Feb-08	45	109	–	86.24	–
	2019-Feb-09	26	104	–	86.19	–
Position-5	2019-Feb-06	16	101	142	86.34	146.97
	2019-Feb-07	35	92	125	86.29	146.92
	2019-Feb-10	38	116	–	86.15	–

^a Tuning frequencies of the Local oscillator (LO) during the observations.

3. RESULTS

From the calibrated spectra data, we identify different transitions at each pointing position according to their rest frequency, which is listed in Table 3. Figures 2-4 present spectra of $\text{H}^{13}\text{CN } J=1-0$, $\text{HC}^{15}\text{N } J=1-0$, $\text{H}^{13}\text{CO}^+ J=1-0$, $\text{HN}^{13}\text{C } J=1-0$, $\text{H}^{15}\text{NC } J=1-0$, and $\text{HC}_3\text{N } J=10-9$ covered by the 3-mm band, while $\text{H}_2\text{CO } J=2-1$ is covered by the 2-mm band. The intensities of all spectra are plotted on the T_{MB} scale. For comparison, spectra of the major isotopologues of HCN $J=1-0$, $\text{HCO}^+ J=1-0$ or HNC $J=1-0$ are overlaid.

Most spectra, especially those from main isotopologues, at position-3 (hereafter P3; the central position) show two velocity components, which has been also shown in Salas et al. (2014) and Li et al. (2020). Only a single velocity component can be

Table 3. Integrated Intensities at All Positions

Line	ν_{rest} (GHz)	I (K km s ⁻¹)									
		Position-1			Position-2		Position-3		Position-4		Position-5
		Blue-shifted	Blue-shifted	Red-shifted	Blue-shifted	Red-shifted	Blue-shifted	Red-shifted	Blue-shifted	Red-shifted	Red-shifted
HC ¹⁵ N 1-0	86.055	0.08 ± 0.025	0.29 ± 0.04	< 0.11	0.29 ± 0.02	0.24 ± 0.02	–	< 0.08	< 0.08		
H ¹³ CN 1-0	86.340	0.23 ± 0.05	0.38 ± 0.04	0.27 ± 0.04	0.21 ± 0.04	0.33 ± 0.04	< 0.15	0.30 ± 0.05	0.14 ± 0.02		
SiO 2-1	86.847	< 0.20	< 0.12	–	0.17 ± 0.04	0.25 ± 0.04	–	0.25 ± 0.07	0.29 ± 0.07		
H ¹³ CO ⁺ 1-0	86.754	0.53 ± 0.07	0.80 ± 0.04	0.12	0.50 ± 0.04	0.71 ± 0.04	0.26 ± 0.07	0.68 ± 0.07	0.36 ± 0.07		
HCO 1-0	86.670	0.45 ± 0.07	0.46 ± 0.04	–	0.27 ± 0.04	0.34 ± 0.04	–	–	< 0.20		
HN ¹³ C 1-0	87.091	< 0.10	< 0.12	–	< 0.08	0.13 ± 0.03	–	0.15 ± 0.05	0.16 ± 0.05		
HCN 1-0	88.632	14.46 ± 0.26	19.63 ± 0.04	6.04 ± 0.04	11.57 ± 0.04	15.47 ± 0.04	3.71 ± 0.03	21.09 ± 0.03	14.26 ± 0.06		
H ¹⁵ NC 1-0	88.866	< 0.09	< 0.12	–	–	< 0.15	–	< 0.10	< 0.18		
HCO ⁺ 1-0	89.189	22.29 ± 0.04	30.23 ± 0.04	8.14 ± 0.04	18.16 ± 0.05	22.64 ± 0.05	6.18 ± 0.04	29.89 ± 0.04	19.69 ± 0.05		
HNC 1-0	90.663	6.60 ± 0.03	9.67 ± 0.05	2.45 ± 0.05	6.00 ± 0.05	7.13 ± 0.05	1.74 ± 0.03	9.68 ± 0.03	5.82 ± 0.05		
HC ₃ N 10-9	90.979	0.64 ± 0.03	1.19 ± 0.04	0.40 ± 0.04	0.65 ± 0.03	1.06 ± 0.03	0.11 ± 0.03	1.14 ± 0.03	0.61 ± 0.04		
H ₂ CO 2-1	145.603	1.73 ± 0.06	2.86 ± 0.08	–	0.67 ± 0.07	2.35 ± 0.07	0.17 ± 0.05	3.22 ± 0.05	1.40 ± 0.06		

Notes: Velocity-integrated intensities are calculated with fixed velocity ranges of 0–200 km s⁻¹ and 200–400 km s⁻¹ for the blue-shifted and the red-shifted component, respectively. Errors of the velocity-integrated intensities are calculated with $\Sigma(I) = \sigma_{\text{line-free}}^{\text{chan}} \times \sqrt{\Delta V \delta v}$, where $\sigma_{\text{line-free}}^{\text{chan}}$ is the r.m.s. noise level obtained from the line-free channels at the corresponding velocity resolution; δv is the velocity resolution (36 km s⁻¹); ΔV is the line width (200 km s⁻¹).

identified from the line profiles at all four off-centre positions. Among them, positions-1 and -2 (hereafter P1 & P2; at the south-west side) are dominated by the blue-shifted velocity component, while positions-4 and -5 (hereafter P4 & P5; at the north-east side) are dominated by the red-shifted velocity component, respectively.

3.1. Detected lines

As shown in Li et al. (2020), the spectra at P3 can be fitted with two-component Gaussian profiles. However, the velocity difference between the two components may not be constant among all five positions, and the outcome of the two-component Gaussian fitting strongly depends on the data quality. Therefore, we calculate the velocity-integrated intensities of all molecular lines in two fixed velocity ranges, i.e., 0–200 km s⁻¹ and 200–400 km s⁻¹, for the blue-shifted and the red-shifted component, respectively. Table 3 presents the velocity-integrated intensities at all positions. For P1 and P5, only the major velocity component is considered, because of the weakness of the minor component. Although some lines show emission line features on $\sim 2\text{-}\sigma$ levels, we only adopt $3\text{-}\sigma$ at their upper limits. In the following, we present properties of each isotopologue line.

- **H¹³CN $J=1\rightarrow 0$, HN¹³C $J=1\rightarrow 0$, and H¹⁵NC $J=1\rightarrow 0$:**

We present the line profile of H¹³CN $J=1\rightarrow 0$ in the left panel of Figure 2. H¹³CN $J=1\rightarrow 0$ is detected at all five positions. Two velocity components are detected at three central positions, P2, P3, and P4. At P4, the blue-shifted component only shows a weak feature at $\sim 2\text{-}\sigma$ level. Therefore, we present $3\text{-}\sigma$ upper limits for it in Table 3. HN¹³C $J=1\rightarrow 0$ is detected in P3, P4, and P5, which is shown in the middle panel of Figure 3. The north-east (NE) side shows stronger HN¹³C emission than those at the south-west (SW) side. H¹⁵NC $J=1\rightarrow 0$ is not detected at all positions, which is shown in the right panel of Figure 3. So, we show $3\text{-}\sigma$ upper limits of the velocity-integrated intensities in Table 3.

- **HC¹⁵N $J=1\rightarrow 0$:**

We present the line profile of HC¹⁵N $J=1\rightarrow 0$ in the left panel of Figure 3. HC¹⁵N $J=1\rightarrow 0$ is blended with SO $J=2\rightarrow 1$, with only a 200 km s⁻¹ offset in velocity. This line blending effect is mostly severe at P3, where SO $J=2\rightarrow 1$ peak is at the same level of HC¹⁵N $J=1\rightarrow 0$ (see Figure 3). At all other four positions, however, HC¹⁵N $J=1\rightarrow 0$ emission seems not heavily polluted by the SO $J=2\rightarrow 1$ emission, possibly because the SO emission is only enhanced in the central shocked region (Pineau des Forets et al. 1993; Aladro et al. 2011b). Therefore, we use the HCN line profile at P3 as a template and fit the SO profile at the same position, then remove the fitted SO contribution. We then use the residual to derive the integrated intensity of HC¹⁵N at P3. For P4 & P5, we estimate $3\text{-}\sigma$ upper limits for the velocity-integrated intensities. Comparing with the spatial variation of H¹³NC $J=1\rightarrow 0$, HC¹⁵N $J=1\rightarrow 0$ show a contrary trend along the major axis.

- **H¹³CO⁺ $J=1\rightarrow 0$, HCO $J=1\rightarrow 0$ and SiO $J=2\rightarrow 1$:**

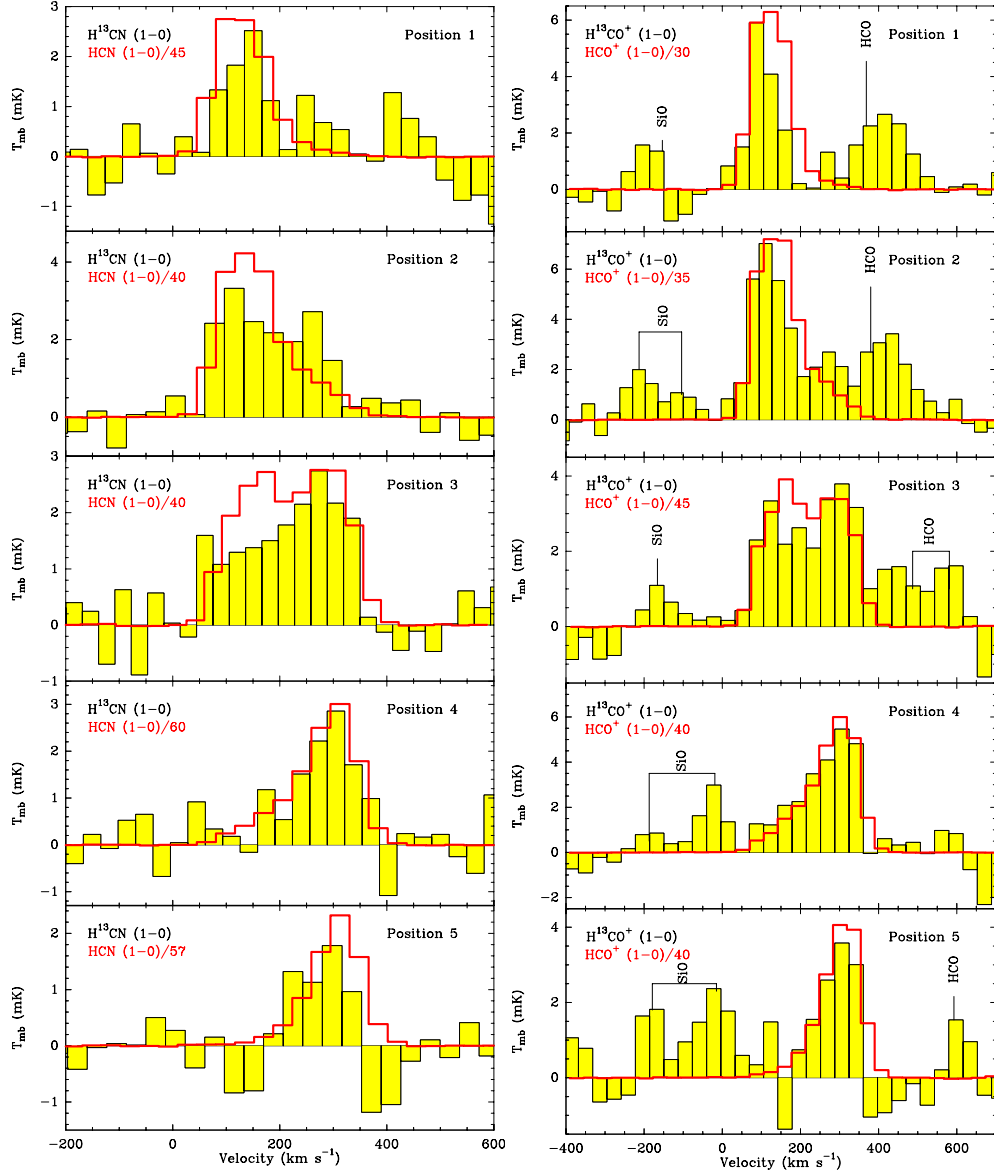


Figure 2. $\text{H}^{13}\text{CN } J=1-0$ (left) and $\text{H}^{13}\text{CO}^+ J=1-0$ (right) spectra (black histograms filled in yellow) measured at five positions along the major axis of M 82. The HCN and $\text{HCO}^+ J=1-0$ spectra are overlaid as red lines, after being normalised to roughly the same peak intensities as the isotopic lines. The velocity resolution is $\sim 35 \text{ km s}^{-1}$ for all spectra. The right panel has a slightly larger velocity range to present the SiO and HCO spectra.

As shown in the right panel of Figure 2, $\text{H}^{13}\text{CO}^+ J=1-0$ is detected at all five positions. $\text{HCO } J=1-0$ and $\text{H}^{13}\text{CO}^+ J=1-0$ have a velocity offset of 294 km s^{-1} , therefore they show a weak blending at P2 and P3. The HCO $J=1-0$ line is well detected in the SW side, while in the NE side it was only marginally detected at P5.

SiO $J=2-1$ seems not blended with $\text{H}^{13}\text{CO}^+ J=1-0$. SiO $J=2-1$ is stronger at the NE side than that at the SW side, where we only obtain $3\text{-}\sigma$ upper limits at P1& P2. This asymmetric distribution of SiO indicates a fast shock at the NE side, possibly driven by outflow (Gusdorf et al. 2008; Gibb & Hoare 2007; López-Sepulcre et al. 2011).

- **$\text{HC}_3\text{N } J=10\rightarrow 9$:**

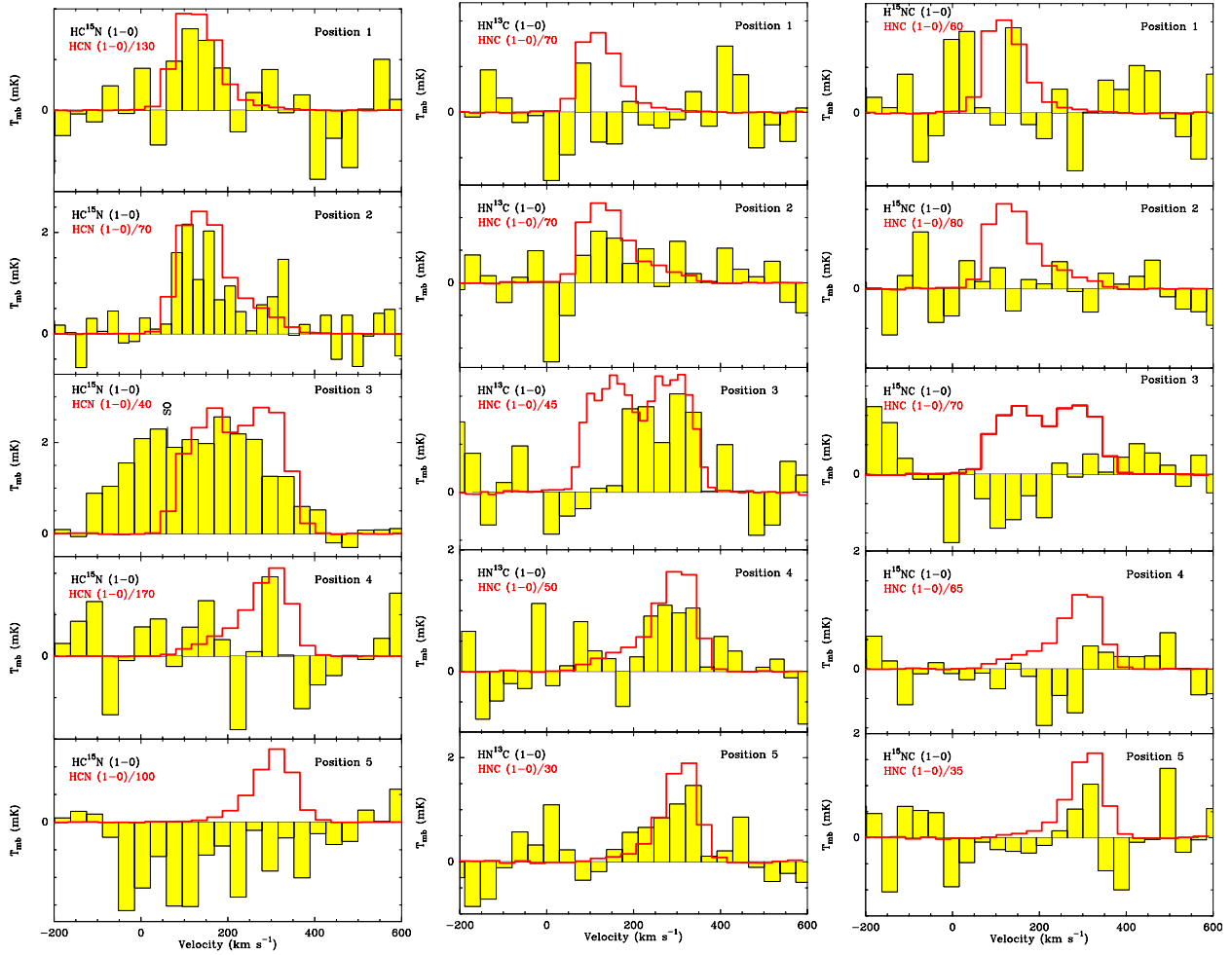


Figure 3. HC^{15}N $J=1-0$ (left), HN^{13}C $J=1-0$ (middle) and H^{15}NC $J=1-0$ (right) spectra (black histograms filled in yellow) measured at five positions along the major axis of M82. The HCN and HNC $J=1-0$ spectra are overlaid as red lines, after being normalised to roughly the same peak intensities as the isotopic lines. The velocity resolution is $\sim 35 \text{ km s}^{-1}$ for all spectra.

We present the line profile of HC_3N $J=10-9$ in the left panel of Figure 4. Being optically-thin in most galactic environments (Morris et al. 1976), HC_3N 10-9 is detected at all positions. This line is stronger than those isotopologue lines of other dense gas tracers at the same position. The line profile of HC_3N is similar to that of HCN $J=1\rightarrow 0$ at each position. The velocity-integrated intensity of HC_3N $J=10-9$ at P-2 is consistent with that reported by Aladro et al. (2015).

- **H_2CO $J=2(0,2)-1(0,1)$:** We present the line profiles of H_2CO $J=2(0,2)-1(0,1)$ in the middle panel of Figure 4. Most of the emission feature around 145.603 GHz seems from H_2CO $J=2(0,2)-1(0,1)$, whose frequency fits the line profile very well. However, HC_3N $J=16-15$ might also contribute part of the flux to the red-shift emission feature.
- **HCN, HCO^+ , and HNC $J=1-0$:** HCN, HCO^+ and HNC $J=1-0$ are all detected with high signal to noise level, at all five positions. Their line profiles agree well with each other at the same positions (see Figure 4). All these lines show double-peak profiles at the central position, which is not always seen in those weak isotopologue lines.

3.2. Line Intensity Ratios

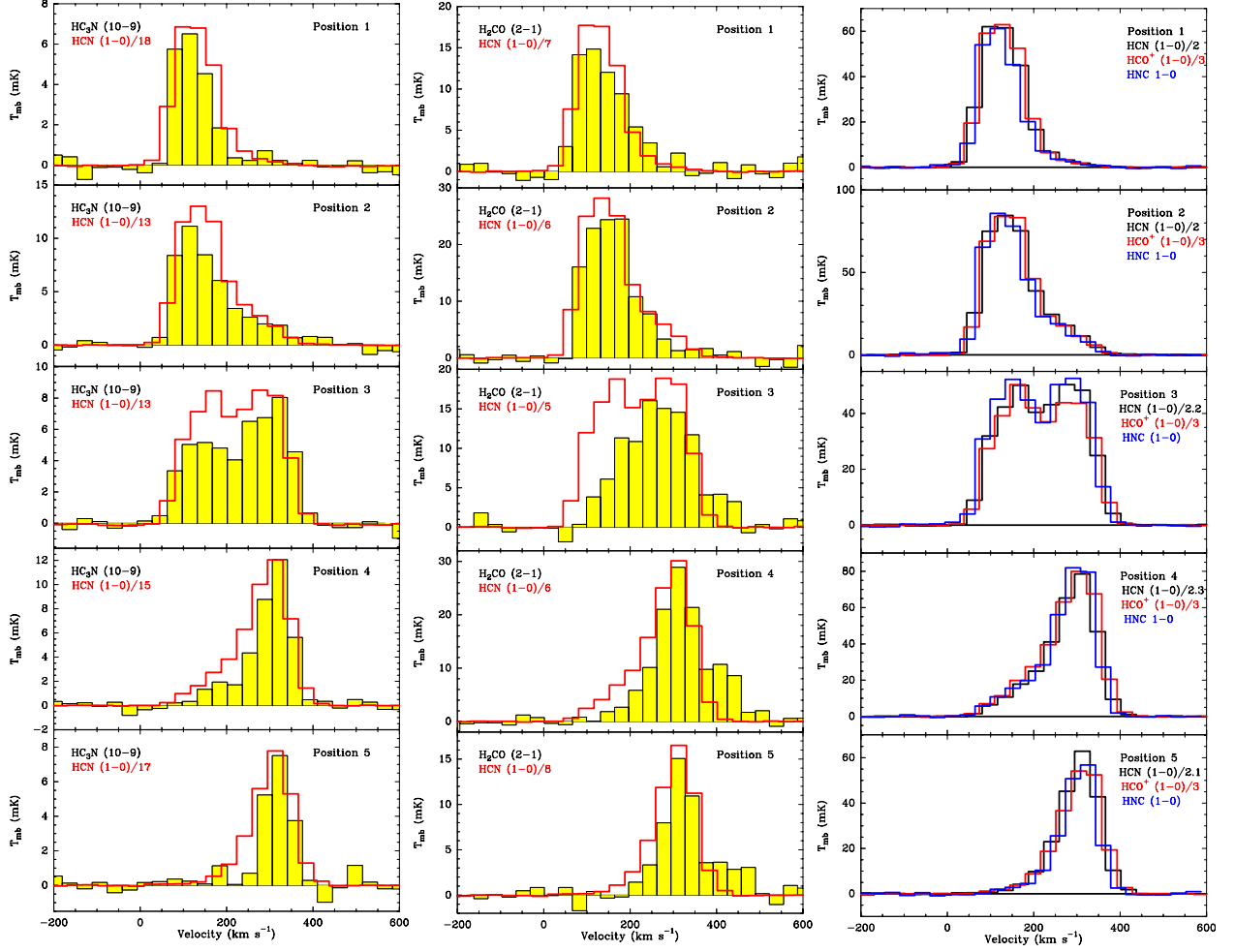


Figure 4. $\text{HC}_3\text{N } J=10-9$ (Left), $\text{H}_2\text{CO } 2-1$ (middle) spectra, shown as black histograms filled in yellow, measured at five positions along the major axis of M 82. The HCN, HCO^+ , and HNC $J=1-0$ spectra are overlaid with black, red, and blue lines, respectively. They are normalised to roughly the same peak intensities. The velocity resolution is $\sim 35 \text{ km s}^{-1}$ for all spectra.

With all measured velocity-integrated intensities, we obtained line intensity ratios between the main and rare isotopologue lines of HCN, HCO^+ , and HNC at each position, and we list results in Table 4. At the central position (P-3), we calculated ratios obtained from three velocity-integrated intensities, i.e., blue-shifted, red-shifted, and total velocity components of these lines.

As shown in Table 4, the ratios of $I(\text{H}^{13}\text{CO}^+)/I(\text{H}^{13}\text{CN})$ and $I(\text{H}^{13}\text{CN})/I(\text{HC}_3\text{N})$ seem relatively constant among all positions, with a variation $\sim 20-30\%$. However, most other intensity ratios show a significant spatial variation, which can reach up to a factor of 4–5 (see Figure 5). The spatial variation of $I(\text{HCN})/I(\text{H}^{13}\text{CN})$, $I(\text{HCO}^+)/I(\text{H}^{13}\text{CO}^+)$, and $I(\text{HCN})/I(\text{HC}^{15}\text{N})$ ratios follow a similar trend, with higher values at the NE side than those at the SW side. These ratios in the central region are lower than those on the disk. These trends are consistent with **what has been** found in $I(^{12}\text{CO})/I(^{13}\text{CO}) J=1-0$ (Kikumoto et al. 1998). However, the $I(\text{HNC})/I(\text{HN}^{13}\text{C})$ intensity ratios show an opposite trend along the major axis, compared with others.

3.3. Optical depths of the main isotopologue lines

Under the assumptions of local thermal equilibrium (LTE), uniform gas excitation, constant isotopic abundance ratios, and neglecting radiative transfer by the cosmic microwave background, we can derive optical depths of the main isotopic lines. We adopt the same method as reported in Li et al. (2020), in which the line ratio R and the optical depth for a specific isotopologue line τ , is related as $R = (1 - e^{-\tau_{12}})/(1 - e^{-\tau_{13}})$

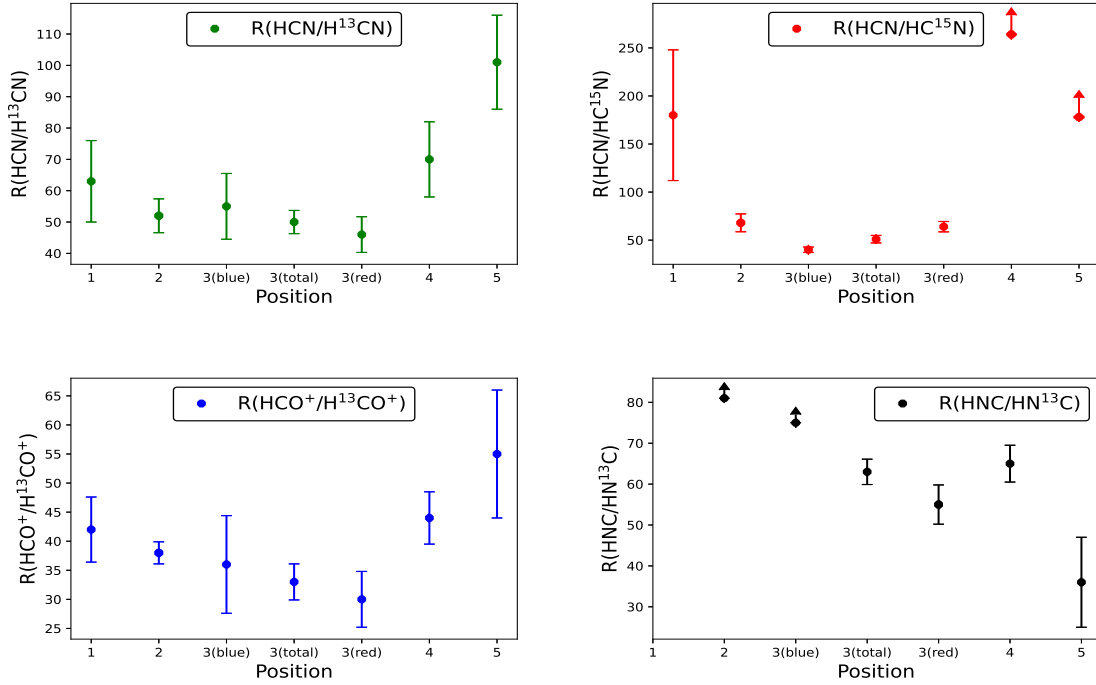


Figure 5. The isotopic ratios as a function of Positions. These isotopic ratios are $I(\text{HCN})/I(\text{H}^{13}\text{CN})$, $I(\text{HCN})/I(\text{HC}^{15}\text{N})$, $I(\text{HCO}^+)/I(\text{H}^{13}\text{CO}^+)$, and $I(\text{HNC})/I(\text{HN}^{13}\text{C})$, respectively

Due to the large uncertainty of absolute abundance ratio of isotopes in external galaxies, we adopt various $^{12}\text{C}/^{13}\text{C}$ and $^{14}\text{N}/^{15}\text{N}$ abundance ratios reported in the literature: $^{12}\text{C}/^{13}\text{C} = 89$ (the Solar system, Clayton & Nittler 2004) and 200 (Ultra-Infrared-luminous ULIRGs, Romano et al. 2017), and $^{14}\text{N}/^{15}\text{N} = 100$ (nearby starburst galaxies, Chin et al. 1999), 200 (Galactic massive star-forming regions, Li et al. 2017), and 290 (the Solar neighbourhood at $R_{\text{gc}} \sim 7.9$ kpc, Adande & Ziurys 2012). Table 5 shows the derived optical depths of HCN, HCO⁺, and HNC $J = 1 \rightarrow 0$.

The optical depths of HCN $J=1-0$ and HCO⁺ $J=1-0$ only have a slight variation along the major axis of M 82, with higher optical depths in the central region than those on the two sides of the disk. The observed $I(\text{HCN})/I(\text{H}^{13}\text{CN})$ $J=1-0$ line ratio could exceed the assumed $^{12}\text{C}/^{13}\text{C}$ abundance ratio occasionally, meaning that the actual $^{12}\text{C}/^{13}\text{C}$ ratio should be even higher. Therefore, the optical depths calculated with $^{12}\text{C}/^{13}\text{C} = 89$ are the lower limits, making $\tau_{\text{HCN}J=1-0} > 1$ at most positions. This also applies to the $\tau_{\text{HCN}J=1-0}$ calculated with the assumptions of various $^{14}\text{N}/^{15}\text{N}$ abundance ratios. Due to limited sensitivity, we can only obtain optical depths of HNC $J=1-0$ at three positions.

3.4. Constraints on $^{12}\text{C}/^{13}\text{C}$ and $^{14}\text{N}/^{15}\text{N}$ Abundance Ratios

To obtain optical depths accurately, one should also consider the possible radial gradient of $^{12}\text{C}/^{13}\text{C}$ abundance ratio, which increases radially in our Milky Way. This is currently not possible due to the lack of abundance measurements. However, our newly measured line ratios between the isotopologues can still be used to set tight constraints on the abundance ratios. The observed HCN/H¹³CN line ratio reaches 101 ± 15 , which is higher than the $^{12}\text{C}/^{13}\text{C}$ abundance ratio in the Solar neighbourhood (~ 89). But it is consistent with the values measured in the outer Galactic disk regions (Milam et al. 2005).

With the double isotope method (Adande & Ziurys 2012), the $^{14}\text{N}/^{15}\text{N}$ ratio can be calculated using the line ratio of $I(\text{H}^{13}\text{CN})/I(\text{HC}^{15}\text{N})$ and the $^{12}\text{C}/^{13}\text{C}$ abundance ratio, by $^{14}\text{N}/^{15}\text{N} = I(\text{H}^{13}\text{CN})/I(\text{HC}^{15}\text{N}) \times ^{12}\text{C}/^{13}\text{C}$. Assuming $^{12}\text{C}/^{13}\text{C} = 89$ in at SW side and at the center, average values of $^{14}\text{N}/^{15}\text{N}$ ratios are 186 ± 113 and 91 ± 11 , respectively. On the other hand, at the NE side, adopting $^{12}\text{C}/^{13}\text{C} = 89$, the lower limits of $^{14}\text{N}/^{15}\text{N}$ ratios range from 156 to 334.

4. DISCUSSION

4.1. Comparison with data in the literature

Table 4. Intensity ratios of the isotopologues of HCN, HNC and HCO⁺

Position	$I(\text{HCN})/I(\text{H}^{13}\text{CN})$	$I(\text{HCN})/I(\text{HC}^{15}\text{N})$	$I(\text{HCO}^+)/I(\text{H}^{13}\text{CO}^+)$	$I(\text{HNC})/I(\text{HN}^{13}\text{C})$	$I(\text{H}^{13}\text{CN})/I(\text{HC}^{15}\text{N})$	$I(\text{H}^{13}\text{CO}^+)/I(\text{H}^{13}\text{CN})$	$I(\text{H}^{13}\text{CN})/I(\text{HC}_3\text{N})$
	$J=1-0$	1-0	1-0	1-0	1-0	1-0	1-0/10-9
1	63 ± 14	180 ± 68	42 ± 6	> 66	2.89 ± 1.25	2.30 ± 1.25	0.36 ± 0.08
2	52 ± 5	68 ± 9	38 ± 2	> 81	1.31 ± 0.23	2.10 ± 0.23	0.32 ± 0.04
3 _a	55 ± 11	40 ± 3	36 ± 3	> 75	0.72 ± 0.15	2.38 ± 0.15	0.32 ± 0.06
3 _b	46 ± 6	64 ± 5	32 ± 2	55 ± 13	1.37 ± 0.20	2.15 ± 0.20	0.31 ± 0.04
3 _{total}	51 ± 6	52 ± 3	34 ± 2	> 65	1.02 ± 0.13	2.24 ± 0.13	0.32 ± 0.02
4	70 ± 12	> 264	44 ± 5	65 ± 22	> 3.75	2.26 ± 0.44	0.26 ± 0.04
5	101 ± 15	> 178	55 ± 11	36 ± 11	> 1.75	2.57 ± 0.62	0.23 ± 0.04

Note. To keep uniformity, we only calculate the intensity ratio of one velocity component.

^a The ratios of the blue-shifted emission are estimated for positions-1 and -2.

^b For positions-3, -4, and -5, the red-shifted emission are used to calculate the ratios.

Table 5. Optical depths for HCN, HNC, and HCO⁺

Position	$\tau(\text{HCN})^a$ (1-0)		$\tau(\text{HNC})^b$ (1-0)		$\tau(\text{HCO}^+)^c$ (1-0)		$\tau(\text{HCN})^d$ (1-0)		
	89 ^e	200 ^e	89	200	89	200	100 ^f	200 ^f	290 ^f
1	0.75 ± 0.52	3.05 ± 0.82	< 0.64	< 2.88	1.78 ± 0.38	4.78 ± 0.68	–	0.22 ± 0.01	1.05 ± 0.13
2	1.21 ± 0.27	3.79 ± 0.44	< 0.19	< 2.21	2.07 ± 0.15	5.31 ± 0.28	0.84 ± 0.39	2.77 ± 2.18	4.23 ± 1.40
3 _a	1.07 ± 0.48	3.57 ± 0.79	< 0.36	< 2.45	2.24 ± 0.26	5.61 ± 0.75	2.27 ± 1.40	5.03 ± 3.10	7.34 ± 2.28
3 _b	1.52 ± 0.34	4.34 ± 0.58	1.07 ± 0.02	3.57 ± 0.03	2.62 ± 0.18	6.34 ± 0.56	0.98 ± 0.45	2.99 ± 2.27	4.51 ± 1.50
3 _{total}	1.26 ± 0.19	3.88 ± 0.47	< 0.75	< 3.05	2.41 ± 0.15	5.95 ± 0.31	1.51 ± 1.21	3.80 ± 2.61	5.61 ± 1.82
4	0.51 ± 0.38	2.68 ± 0.58	0.67 ± 0.81	2.93 ± 1.3	1.65 ± 0.28	4.55 ± 0.5	–	–	< 0.19
5	–	1.58 ± 0.40	2.24 ± 0.03	5.61 ± 0.05	1.07 ± 0.49	3.57 ± 0.8	–	< 0.24	< 1.07
mean	1.11 ± 1.51	3.64 ± 2.64	< 0.75	< 3.05	1.78 ± 0.98	4.78 ± 1.79	< 1.11	< 0.9	< 2.12
whole	1.16 ± 0.15	3.72 ± 0.24	< 0.64	< 2.88	1.92 ± 0.11	4.03 ± 0.21	< 1.87	< 1.9	< 3.05

a The optical depth of HCN is calculated by the ratio of HCN/H¹³CN.

a The optical depth of HNC $J=1-0$ is calculated by the ratio of HNC/HN¹³C $J=1-0$.

b The optical depth of HCO⁺ 1-0 is calculated by the ratio of HCO⁺/H¹³CO⁺ 1-0.

d The optical depth of HCN is calculated by the ratio of HCN/HC¹⁵N.

e Abundance ratios of ¹²C/¹³C: 89 (Solar system (Clayton & Nittler 2004)) and 200 (ULIRGs (Romano et al. 2017)).

f Abundance ratios of ¹⁴N/¹⁵N: 100 (nearby starburst galaxies (Chin et al. 1999)), 200 (Galactic massive star-forming regions (Li et al. 2017)) and 290 (local interstellar medium (Adande & Ziurys 2012)).

Table 6 summarizes literature measurements of $I(\text{HCN})/I(\text{H}^{13}\text{CN})$ $J=1-0$, $I(\text{HCO}^+)/I(\text{H}^{13}\text{CO}^+)$ $J=1-0$, and $I(\text{HNC})/I(\text{HN}^{13}\text{C})$ $J=1-0$ from nearby galaxies, including starburst galaxies, ULIRGs and active galactic nucleus (AGN)-dominated galaxies. All these ratios in M 82 are higher than those found in the literature, except for M 83.

Previous observations of dense gas tracers have shown that they are mostly optically thick in both Galactic giant molecular clouds (GMCs) and external galaxies (Wang et al. 2014; Meier et al. 2015; Jiménez-Donaire et al. 2017; Li et al. 2017, 2020). If we assume that the abundance ratio of ¹²C/¹³C is 40, which is obtained as the average condition of nearby galaxies (Henkel et al. 1994, 2010), the HCN, HCO⁺ and HNC lines of M 82 would be optically thin.

At all five positions in M 82, ratios of $I(\text{H}^{13}\text{CN})/I(\text{H}^{13}\text{CO}^+)$ $J=1-0$ are lower than those of $I(\text{HCN})/I(\text{HCO}^+)$ $J=1-0$. Similar results for the $J=2-1$ transition were also reported by Aladro et al. (2011b) at P2, where the $I(\text{H}^{13}\text{CN})/I(\text{H}^{13}\text{CO}^+)$ $J=2-1$ ratio is lower than that of $I(\text{HCN})/I(\text{HCO}^+)$ $J=2-1$. This indicates that HCN lines should have lower optical depths than those of HCO⁺ lines.

4.2. Optical Depths

Given the high intensity ratios of $I(\text{HCN})/I(\text{H}^{13}\text{CN})$ $J=1-0$ in a range from 51 ± 6 to 101 ± 15 at all five positions, a ¹²C/¹³C abundance ratio of 40 (Henkel et al. 1998) can not be valid. Kikumoto et al. (1998) and Tan et al. (2011) also found similar results,

Table 6. Integrated intensity ratios from the literature

Galaxy	$\frac{\text{HCN}}{\text{H}^{13}\text{CN}}$ 1-0	$\frac{\text{HCO}^+}{\text{H}^{13}\text{CO}^+}$ 1-0	$\frac{\text{HNC}}{\text{HN}^{13}\text{C}}$ 1-0	Type	Reference
NGC 3079	10±5	7±2	>28	SB/AGN	1
Mrk 231	16±5	12±5	>7	SB	1
NGC 4418	8±3	–	–	SB/AGN	2
NGC 1068	16±1	20±1	38±6	AGN	3
NGC 3351	21±3	>17	–	SB(r)b	4
NGC 3627	7±1	>12	–	SB/AGN	4
NGC 253	17±1	24±2	–	SB	4
M 83	41±7	44±13	–	SAB(s)c	5
NGC 5194	27±18	34±29	>16	SB/AGN	6
M 82	46±6–101±15	32±2–55±11	36±11–65±22	SB	this work

References: (1)Li et al. (2020) (2) Costagliola et al. (2011) (3) Wang et al. (2014) (4)Jiménez-Donaire et al. (2017) (5)Aladro et al. (2015) (6)Watanabe et al. (2014) (7)Muller et al. (2011).

and they adopted a $^{12}\text{C}/^{13}\text{C}$ abundance ratio of 60. No matter which $^{12}\text{C}/^{13}\text{C}$ abundance ratio is adopted, ^{12}C -bearing dense gas tracer lines need to have at least moderate optical depths.

The optical depths of dense gas tracers may be decreased by the feedback of supernova explosions in M 82, which has been found to in previous studies (Allen & Kronberg 1998; Mattila & Meikle 2001). Such supernova feedback strongly affect the molecular gas environments, which can be seen from strong SiO emission (see Figure 2), high H_2 1-0 $S(1)/\text{Br}\gamma$ ratio, and high ratio of $I(^{12}\text{CO})/I(^{13}\text{CO})$ (Lester et al. 1990; Mouri et al. 1989). Therefore, the ^{12}C -bearing molecular lines would be expected to be more optically thin, because the shock conditions could broaden the lines, which have an increased escape probability in radiative transfer. Such effects have been seen in Galactic supernova remnant, which are interacting with molecular clouds (e.g., Zhang et al. 2010),

To mimic spatially unresolved galaxies, we further derive the weighted mean optical depths of dense gas tracers in M 82, by averaging optical depths among all positions, weighted with their line fluxes (see Table 5 marked as “mean”). The unweighted mean optical depth, which was obtained directly from the total flux ratios, is also listed in the same tables (marked as “whole”). Both “mean” and “whole” optical depths agree well with those obtained on the disk, within the error bars. Thus, for galaxies without spatially information, optical depths of dense gas tracers obtained from a whole galaxy could generally represent average conditions on the disk.

4.3. The $^{12}\text{C}/^{13}\text{C}$ abundance ratio

The two isotopes of Carbon, ^{12}C and ^{13}C , have different mechanisms of nucleosynthesis. The main isotope, ^{12}C , could be partly produced by the triple- α reaction in massive stars ($> 8 M_{\odot}$, Wilson & Matteucci 1992; Nomoto et al. 2013), and partly by lower mass stars. Therefore, ^{12}C can increase quickly after the starburst starts, due to the short lifetime of massive stars. Most of ^{13}C , on the other hand, is formed in low- and intermediate-mass stars ($< 8 M_{\odot}$), which means that most ^{13}C should be released to the ISM on much longer timescales than that of ^{12}C (Wilson & Matteucci 1992; Hughes et al. 2008).

As a result, the $^{12}\text{C}/^{13}\text{C}$ abundance ratio could represent the star-formation history (Wilson & Rood 1994; Henkel et al. 2010) — high ratios for long-term starbursts (a few hundreds of Myrs) and low ratios for young starbursts (tens of Myrs), before the low-mass stars start to release ^{13}C .

Given the relatively short starburst timescales of M 82 ($\sim 5 \times 10^7$ yr, Konstantopoulos et al. 2009), the majority of the newly born low-mass stars are still alive. So, the $^{12}\text{C}/^{13}\text{C}$ ratio can be enhanced in the central regions, where starburst is more intensive compared to that in the outer disk. Therefore, the current starbursts generate the $^{12}\text{C}/^{13}\text{C}$ decreasing trend from center to outskirt along the major axis of M 82.

However, the observed $^{12}\text{C}/^{13}\text{C}$ ratios are not only contributed from the current starbursts contribution, but also produced from all the past starburst activities in history. Besides, Galactic chemical evolution models predict that the $^{12}\text{C}/^{13}\text{C}$ ratio would vary by a factor of two, even if a strong starburst produce half of the stellar mass in a secular evolving galaxy (Romano et al. 2017). Even if the undergoing starburst could slightly enhance $^{12}\text{C}/^{13}\text{C}$ abundance ratio in a short timescale in the central region during the starburst, it would not change the increasing $^{12}\text{C}/^{13}\text{C}$ gradient in M 82, similar to the Milky Way.

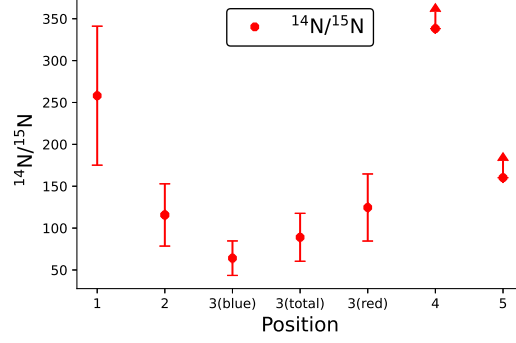


Figure 6. The abundance ratio of $^{14}\text{N}/^{15}\text{N}$ as a function of positions.

4.4. The $^{14}\text{N}/^{15}\text{N}$ abundance ratio

In external galaxies, the $^{14}\text{N}/^{15}\text{N}$ abundance ratios have been measured in a range from ~ 100 to ~ 450 (Henkel et al. 1998, 2018; Wang et al. 2014, 2016; Adande & Ziurys 2012). This ratio measured in two starbursts, NGC 4945 (~ 200 –400, Henkel et al. 2018) and ULIRG Arp 220 (440^{+140}_{-82} , Wang et al. 2014), are higher than those found in M 82 (~ 80 –250, see Figure 6). In our Milky Way, the $^{14}\text{N}/^{15}\text{N}$ ratios distribute in a large range (100–600, Li et al. 2017), with a possible positive gradient from the center to out disk (Chen et al. 2021).

Figure 6 shows estimated $^{14}\text{N}/^{15}\text{N}$ ratios as a function of galactocentric distance. If we adopt an assumption of constant $^{12}\text{C}/^{13}\text{C}$ abundance ratio of 89, $^{14}\text{N}/^{15}\text{N}$ abundance ratios tend to increase with galactocentric distance, which is consistent with the $^{14}\text{N}/^{15}\text{N}$ gradient found in the Milky Way (Dahmen et al. 1995; Adande & Ziurys 2012; Romano & Matteucci 2003; Romano et al. 2017; Chen et al. 2021).

On the other hand, the $^{12}\text{C}/^{13}\text{C}$ abundance ratio shows an increasing gradient from the center to the outer disk in the Milky Way (Wilson & Rood 1994; Savage et al. 2002; Milam et al. 2005; Yan et al. 2019). If we adopt a similar positive $^{12}\text{C}/^{13}\text{C}$ abundance gradient to M 82, which is consistent with the prediction in Section 4.3, the $^{14}\text{N}/^{15}\text{N}$ abundance ratio would show an even stronger gradient, with lower values in the center and higher ratios on the disk.

4.5. Astrochemical effects

Selective photon dissociation prefers to destroy ^{13}C - and ^{15}C -bearing molecules, which would increase $^{12}\text{C}/^{13}\text{C}$ and $^{14}\text{N}/^{15}\text{N}$ abundance ratios in high UV fields (Wilson & Matteucci 1992; Savage et al. 2002). However, the inner region of M 82 has lower $I(\text{HCO}^+)/I(\text{H}^{13}\text{CO}^+)$ and $I(\text{HCN})/I(\text{HC}^{15}\text{N})$ line values, indicating that photo-dissociation does not play a key role.

Isotope fractionation, which could enhance $\text{H}^{13}\text{CO}^+/\text{HCO}^+$ and $\text{HC}^{15}\text{N}/\text{HCN}$ ratios, is only effective at a very low temperature (Smith & Adams 1980; Woods & Willacy 2009; Röllig & Ossenkopf 2013; Loison et al. 2019). In M 82, the temperature is relatively high, especially in the center. However, both $I(\text{HCO}^+)/I(\text{H}^{13}\text{CO}^+)$ and $I(\text{HCN})/I(\text{HC}^{15}\text{N})$ ratios increases in the off-center regions, meaning that fractionation effect does not play a key role as well.

5. SUMMARY

In this paper we present results from IRAM 30-m telescope observations along the major axis of M 82 in the 2-mm band and 3-mm band. Four positions are selected to measure the isotopic lines of HCN, HCO^+ , and HNC. The spatial distribution of these optically thin dense gas tracers are obtained, including H^{13}CN , H^{13}CO^+ , HC^{15}N , HN^{13}C , H^{15}NC 1-0. A few other species of SiO $J=2-1$, HCO $J=1-0$, H_2CO $J=2-1$, and HC_3N $J=10-9$ are also detected. We obtain the following results:

(1) H^{13}CN $J=1-0$, H^{13}CO^+ $J=1-0$, HC_3N $J=10-9$ and H_2CO $J=2-1$ are detected in all four positions along the major axis of M 82. Spectral lines of the transition HC^{15}N $J=1-0$ are not detected at the NE side and HN^{13}C $J=1-0$ emissions are not detected at the SW side. We did not obtain any detection of H^{15}NC $J=1-0$ at all positions. For the tentative detection of the isotopic lines, the 3- σ upper limits are presented.

(2) For spectral line intensity ratios, $I(\text{HCN})/I(\text{H}^{13}\text{CN})$ $J=1-0$, $I(\text{HCO}^+)/I(\text{H}^{13}\text{CO}^+)$ $J=1-0$ and $I(\text{HCN})/I(\text{HC}^{15}\text{N})$ $J=1-0$ show a large spatial variation along the major axis of M 82, which are higher at the NE side than those at the SW side and the value in the central region is lower than that on the disk. However, the $I(\text{HNC})/I(\text{HN}^{13}\text{C})$ ratio seems to show an opposite trend along the major axis.

(3) The optical depths of HCN $J=1-0$ and HCO⁺ $J=1-0$ only have a slight variation along the major axis of M 82, with higher optical depth in the central region than those on the two sides of the disk. Due to limited sensitivity, we can only obtain optical depths of HNC $J=1-0$ at three positions, thus could not summarise any trend for its optical depth variation.

(4) Our measured line ratios between the isotopologues set a lower limit for the abundance ratios of ¹²C/¹³C. Using the double method and $I(\text{H}^{13}\text{CN})/I(\text{HC}^{15}\text{N})$ ratio, the derived ¹⁴N/¹⁵N abundance ratios have an increasing gradient from the center to the outer disk.

ACKNOWLEDGEMENTS

This work is supported by the National Natural Science Foundation of China grant (12041305, 12173067 and 121030243), and the fellowship of China Postdoctoral Science Foundation 2021M691531. We would like to thank P. Salas to provide their data for Figure 1. We are grateful to the staff of IRAM 30-m telescope for their kind help and support during our observations. This study is based on observations carried out under project number 186-18 (PI: Feng Gao) with the IRAM 30-m telescope. IRAM is supported by INSU/CNRS (France), MPG (Germany), and IGN (Spain). We acknowledge the Program for Innovative Talents, Entrepreneur in Jiangsu. We acknowledge the science research grants from the China Manned Space Project with NO.CMS-CSST-2021-A08.

APPENDIX

REFERENCES

- Adande G. R., Ziurys L. M., 2012, *ApJ*, 744, 194
- Aladro R., Martín-Pintado J., Martín S., Mauersberger R., Bayet E., 2011a, *A&A*, 525, A89
- Aladro R., Martín S., Martín-Pintado J., Mauersberger R., Henkel C., Ocaña Flaquer B., Amo-Baladrón M. A., 2011b, *A&A*, 535, A84
- Aladro R., et al., 2015, *A&A*, 579, A101
- Allen M. L., Kronberg P. P., 1998, *ApJ*, 502, 218
- Bayet E., Viti S., Williams D. A., Rawlings J. M. C., 2008, *ApJ*, 676, 978
- Bolato A. D., Wolfire M., Leroy A. K., 2013, *ARA&A*, 51, 207
- Chen J. L., et al., 2021, *ApJS*, 257, 39
- Chin Y.-n., Henkel C., Langer N., Mauersberger R., 1999, *ApJL*, 512, L143
- Clayton D. D., Nittler L. R., 2004, *ARA&A*, 42, 39
- Costagliola F., Aalto S., 2010, *A&A*, 515, A71
- Costagliola F., et al., 2011, *A&A*, 528, A30
- Dahmen G., Wilson T. L., Matteucci F., 1995, *A&A*, 295, 194
- Fuente A., et al., 2008, *A&A*, 492, 675
- Gao Y., Solomon P. M., 2004, *ApJ*, 606, 271
- García-Burillo S., Martín-Pintado J., Fuente A., Neri R., 2001, *ApJL*, 563, L27
- García-Burillo S., Martín-Pintado J., Fuente A., Usero A., Neri R., 2002, *ApJL*, 575, L55
- Gerin M., Goicoechea J. R., Pety J., Hily-Blant P., 2009, *A&A*, 494, 977
- Gibb A. G., Hoare M. G., 2007, *MNRAS*, 380, 246
- Gusdorf A., Pineau Des Forêts G., Cabrit S., Flower D. R., 2008, *A&A*, 490, 695
- Henkel C., Whiteoak J. B., Mauersberger R., 1994, *A&A*, 284, 17
- Henkel C., Chin Y.-N., Mauersberger R., Whiteoak J. B., 1998, *A&A*, 329, 443
- Henkel C., Downes D., Weiß A., Riechers D., Walter F., 2010, *A&A*, 516, A111
- Henkel C., et al., 2018, *A&A*, 615, A155
- Hughes G. L., Gibson B. K., Carigi L., Sánchez-Blázquez P., Chavez J. M., Lambert D. L., 2008, *MNRAS*, 390, 1710
- Jiménez-Donaire M. J., et al., 2017, *MNRAS*, 466, 49
- Kennicutt R. C., Evans N. J., 2012, *ARA&A*, 50, 531
- Kikumoto T., Taniguchi Y., Nakai N., Ishizuki S., Matsushita S., Kawabe R., 1998, *PASJ*, 50, 309
- Kohno K., Kawabe R., Vila-Vilaró B., 1999, *ApJ*, 511, 157
- Konstantopoulos I. S., Bastian N., Smith L. J., Westmoquette M. S., Trancho G., Gallagher J. S. I., 2009, *ApJ*, 701, 1015
- Lada E. A., 1992, *ApJL*, 393, L25
- Lester D. F., Carr J. S., Joy M., Gaffney N., 1990, *ApJ*, 352, 544
- Li S., et al., 2017, *MNRAS*, 466, 248
- Li F., Wang J., Kong M., Li S., 2019, *MNRAS*, 482, 4763
- Li F., Wang J., Fang M., Li S., Zhang Z.-Y., Gao Y., Kong M., 2020, *MNRAS*,
- Loison J.-C., Wakelam V., Gratier P., Hickson K. M., 2019, *MNRAS*, 484, 2747
- López-Sepulcre A., et al., 2011, *A&A*, 526, L2
- Martín S., Martín-Pintado J., Viti S., 2009, *ApJ*, 706, 1323
- Martín S., Aladro R., Martín-Pintado J., Mauersberger R., 2010, *A&A*, 522, A62
- Mattila S., Meikle W. P. S., 2001, *MNRAS*, 324, 325
- Meier D. S., et al., 2015, *ApJ*, 801, 63
- Milam S. N., Savage C., Brewster M. A., Ziurys L. M., Wyckoff S., 2005, *ApJ*, 634, 1126

- Morris M., Turner B. E., Palmer P., Zuckerman B., 1976, *ApJ*, 205, 82
- Mouri H., Taniguchi Y., Kawara K., Nishida M., 1989, *ApJL*, 346, L73
- Mühle S., Seaquist E. R., Henkel C., 2007, *ApJ*, 671, 1579
- Muller S., et al., 2011, *A&A*, 535, A103
- Narayanan D., Krumholz M. R., Ostriker E. C., Hernquist L., 2012, *MNRAS*, 421, 3127
- Nomoto K., Kobayashi C., Tominaga N., 2013, *ARA&A*, 51, 457
- Pety J., 2005, in Casoli F., Contini T., Hameury J. M., Pagani L., eds, SF2A-2005: Semaine de l’Astrophysique Francaise. p. 721
- Pineau des Forets G., Roueff E., Schilke P., Flower D. R., 1993, *MNRAS*, 262, 915
- Rico-Villas F., Martín-Pintado J., González-Alfonso E., Martín S., Rivilla V. M., 2020, *MNRAS*, 491, 4573
- Röllig M., Ossenkopf V., 2013, *A&A*, 550, A56
- Romano D., Matteucci F., 2003, *MNRAS*, 342, 185
- Romano D., Matteucci F., Zhang Z.-Y., Papadopoulos P. P., Ivison R. J., 2017, *MNRAS*, 470, 401
- Salas P., Galaz G., Salter D., Herrera-Camus R., Bolatto A. D., Kopley A., 2014, *ApJ*, 797, 134
- Savage C., Apponi A. J., Ziurys L. M., Wyckoff S., 2002, *ApJ*, 578, 211
- Seaquist E. R., Clark J., 2001, *ApJ*, 552, 133
- Shopbell P. L., Bland-Hawthorn J., 1998, *ApJ*, 493, 129
- Smith D., Adams N. G., 1980, *ApJ*, 242, 424
- Tan Q.-H., Gao Y., Zhang Z.-Y., Xia X.-Y., 2011, *Research in Astronomy and Astrophysics*, 11, 787
- Tanaka K., Nagai M., Kamegai K., Iino T., Sakai T., 2018, *ApJS*, 236, 40
- Tunnard R., et al., 2015, *ApJ*, 800, 25
- Usero A., García-Burillo S., Martín-Pintado J., Fuente A., Neri R., 2006, *A&A*, 448, 457
- Veilleux S., Rupke D. S. N., Swaters R., 2009, *ApJL*, 700, L149
- Wang J., Zhang Z.-Y., Qiu J., Shi Y., Zhang J., Fang M., 2014, *ApJ*, 796, 57
- Wang J., Zhang Z.-Y., Zhang J., Shi Y., Fang M., 2016, *MNRAS*, 455, 3986
- Watanabe Y., Sakai N., Sorai K., Yamamoto S., 2014, *ApJ*, 788, 4
- Wilson T. L., Matteucci F., 1992, *A&A Rv*, 4, 1
- Wilson T. L., Rood R., 1994, *ARA&A*, 32, 191
- Woods P. M., Willacy K., 2009, *ApJ*, 693, 1360
- Yan Y. T., et al., 2019, *ApJ*, 877, 154
- Zhang Z., Gao Y., Wang J., 2010, *Science China Physics, Mechanics, and Astronomy*, 53, 1357

APPENDIX

A. OTHER LINES: SiO $J=2-1$, HCO $J=1-0$, H₂CO $J=2-1$, AND HC₃N $J=10-9$

Apart from the isotopic lines, we also detected a few unique molecular lines, such as SiO $J = 2 \rightarrow 1$, HCO $J = 1 \rightarrow 0$, H₂CO $J = 2 \rightarrow 1$, and HC₃N $J = 10 \rightarrow 9$. These lines offer an excellent opportunity to reveal physical conditions of the ISM of M 82.

A.1. SiO $J=2-1$

SiO, as the shock tracer (Usero et al. 2006), is detected in both the central region and at the NE side, while only 3- σ upper limits are obtained at the SW side. Such result indicates that the shock at the NE side is stronger than that at the SW side. This is consistent with García-Burillo et al. (2001), who found extended off-nuclear SiO $J=2-1$ emission on the NE side, indicating strong molecular shock on large scales. On the other hand, Lester et al. (1990); Mouri et al. (1989) found higher ratio of H₂ 1-0 $S(1)/B_{\text{ry}}$ at the NE side than that at the SW side, consistent with the scenario that the NE shock is stronger. However, the linewidths of HCN, HCO⁺ and HNC do not show obvious differences at both sides, indicating that the shocks may not heavily broaden the linewidth and influence the global properties of dense gas.

A.2. HCO $J=1-0$

As shown on the right panel of Figure 2, HCO $J=1-0$, as a good tracer of PDR (García-Burillo et al. 2002; Gerin et al. 2009; Martín et al. 2009), is stronger at the SW side than that at the NE side. In addition, García-Burillo et al. (2002) also found a giant PDR of ~ 650 pc size in M 82 with HCO 1-0 mapping observation, using the IRAM Plateau de Bure Interferometer. The result suggests that the chemistry of the SW molecular side is dominated by the PDR, which shows typical features of an evolved starburst (Aladro et al. 2011b; Fuente et al. 2008).

A.3. H₂CO $J=2-1$

With high critical density of $1.6 \times 10^6 \text{ cm}^{-3}$ (Kennicutt & Evans 2012), the H₂CO $J=2-1$ transition can also trace dense gas (Bayet et al. 2008), which traces the high-excitation component of the molecular gas in M 82 very well (Mühle et al. 2007). The H₂CO 2-1 emission at the SW side is stronger than that at the NE side, indicating higher excitation conditions at the SW side. Such difference may be caused by the asymmetric outflow (Shopbell & Bland-Hawthorn 1998), which may also impact the NE disk (Seaquist & Clark 2001; Veilleux et al. 2009).

A.4. HC₃N $J=10-9$

As a warm and dense gas tracer (Tanaka et al. 2018), HC₃N can be easily destroyed by UV radiation and Cosmic Rays (Rico-Villas et al. 2020; Costagliola & Aalto 2010). Therefore, HC₃N is mainly excited by collision. HC₃N lines are bright enough to be detected in the local galaxies NGC 4418, NGC 253, IC 342 NGC 6240 and so on (Costagliola et al. 2011; Aladro et al. 2011a; Li et al. 2019). These detections all indicate that the optical depth of HC₃N is very small ($\tau \ll 1$) in most cases, because it has many energy populations.

Assuming similar excitation temperature, the abundance ratio of $I(\text{H}^{13}\text{CN})/I(\text{HC}_3\text{N})$ can be estimated by their intensity ratio. This ratio does not show large variation among different positions, indicating that the distribution of H¹³CN and HC₃N might be uniform along the major axis. The results also implied that the HC₃N emission is either spatially separated from PDRs, or the PDRs might be weak, because UV photons from PDRs can dissociate HC₃N.